NOT PEER-REVIEWED

Research Article

Flexible silicon nanowire bidirectional bending sensors for wearable wrist-posture monitoring

Sheng Wang[1,#,*], Zhenlei Qin[2,#], Yang Gu[2], Xiaopan Song[2,*], Linwei Yu[1,2,*]

[1]College of Electronic and Optical Engineering & College of Flexible Electronics (Future Technology), Nanjing University of Posts and Telecommunications, Nanjing 210023, Jiangsu, China.

[2]School of Electronics Science and Engineering, Nanjing University, Nanjing 210023, Jiangsu, China.

[*]**Correspondence to:** Prof. Linwei Yu, Dr. Sheng Wang, College of Electronic and Optical Engineering & College of Flexible Electronics (Future Technology), Nanjing University of Posts and Telecommunications, Nanjing 210023, Jiangsu, China; School of Electronics Science and Engineering, Nanjing University, Nanjing 210023, Jiangsu, China. E-mail: yulinwei@njupt.edu.cn; shengwang@njupt.edu.cn; Dr. Xiaopan Song, School of Electronics Science and Engineering, Nanjing University, Nanjing 210023, Jiangsu, China. E-mail: songxiaopan@nju.edu.cn

[#]Sheng Wang and Zhenlei Qin contributed equally to this work.

Received: 29 August 2026 | Approved: 02 September 2026 | Online: 02 September 2026

Abstract

Continuous monitoring of wrist posture during resistance exercise can provide feedback on joint alignment and reduce the potential risk of exercise-related injury. However, many existing wearable approaches rely on multiple sensing elements or indirect estimation of joint motion. In this study, we report a morphology-programmable silicon nanowire (SiNW) bending sensor fabricated directly on a flexible polyimide (PI) substrate via the in-plane solid-liquid-solid (IPSLS) mechanism. The wavy SiNW geometry combines mechanical compliance with the piezoresistive response of crystalline silicon, enabling tensile and compressive bending to produce resistance changes of opposite polarity. The resulting sensor exhibited high strain sensitivity in both bending directions and maintained stable responses during repeated deformation. When attached to the dorsal side of the wrist, the sensor distinguished wrist flexion, neutral position, and wrist extension. Placement on the radial or ulnar side enabled radial deviation, neutral position, and ulnar deviation to be resolved. The wirelessly acquired signals were segmented into 1s windows and classified using a lightweight one-dimensional convolutional neural network, achieving accuracies of approximately 98.0% and 97.8% for the two placement-specific tasks. By combining direction-sensitive bending responses with position-dependent wrist sensing, the SiNW bending sensor offers a compact approach for wearable wrist-posture monitoring during exercise.

Keywords: In-plane solid-liquid-solid, silicon nanowire, bending sensor, wearable wrist monitoring, convolutional neural network.

INTRODUCTION

Wrist discomfort and injury are common musculoskeletal concerns in resistance training[1-3]. Under external load, non-neutral wrist postures can redistribute radiocarpal contact forces and can increase local soft-tissue loading[4,5]. More specifically, axial loading of an ulnarly deviated and often pronated wrist is a recognized mechanism of triangular fibrocartilage complex (TFCC) injury[6]. Continuous wrist-posture monitoring can provide objective feedback on alignment during exercise. In routine gym-based resistance training, posture is commonly assessed through visual observation and corrective instruction. Although convenient, visual assessment is affected by viewing angle and temporary occlusion and cannot provide continuous, quantitative tracking[7]. Optical motion-tracking methods can quantify joint kinematics more precisely, but require dedicated capture setups, reliable visibility and controlled imaging geometry, limiting their practicality in everyday gym environments[8,9]. Wearable sensors are better suited to continuous joint posture monitoring during natural exercise. For example, wearable ultrasound can capture detailed internal motion without camera occlusion, but requires acoustic coupling and a more complex array and readout system[10]. Inertial measurement units (IMUs) estimate joint angles from the relative orientations of sensors mounted on body segments adjacent to the joint. However, measurement accuracy can be degraded by gyroscope-bias-induced orientation drift and local magnetic-field disturbances in magnetometer-aided systems[11,12]. Surface electromyography (sEMG) provides complementary information about muscle excitation and can support model-based inference of movement intention, but it does not directly measure joint posture and remains sensitive to electrode placement and limb position[13-15]. These limitations motivate a skin-conformal approach that directly resolves local wrist deformation and its directional variation during loaded exercise.

Bending sensors provide a direct and conformal alternative to wrist-posture monitoring by detecting the tensile and compressive strains associated with local wrist bending. The magnitude and polarity of deformation depend on both the direction of wrist motion and the sensor location, allowing distributed sensors to encode wrist postures through complementary responses[16-18]. Previous bending sensors have employed metallic nanowires, graphene, conducting or piezoelectric polymers, optical waveguide materials[19-24]. For example, Yan *et al.* embedded crossed Ag-nanowire interdigital microelectrodes within a P(VDF-TrFE) piezoelectric film to construct a multidirectional bending sensor, which enabled remote control of a smart car[19]. Zhong *et al.* fabricated a dual-colored, bilayer optical-waveguide bending sensor, enabling calibration-free and bidirectional measurement of bending angles across joints with different curvatures[20].

DOI: 10.20517/scierxiv202609.0756.v1

For multichannel wrist monitoring during loaded exercise, however, the sensors are required to simultaneously provide sufficient sensitivity and operating range, low hysteresis, long-term cyclic stability and reproducible responses across sensing channels[9,25]. Crystalline silicon (c-Si) is attractive for bending sensors due to its large piezoresistive response which enables high strain sensitivity with low electrical hysteresis[26,27]. Nevertheless, the stiffness and brittleness of c-Si necessitate ultrathin membranes and mesh or serpentine layouts for conformal sensing[28,29]. These devices often use Si layers released from costly silicon-on-insulator (SOI) wafers and transfer-printed onto compliant substrates, adding patterning and assembly steps[30]. Scalable manufacturing of high-sensitivity c-Si bending sensors with programmable geometries therefore remains challenging.

To address this challenge, we propose a wrist-posture monitoring approach using a bending sensor based on silicon nanowires (SiNWs) grown through a novel in-plane solid-liquid-solid (IPSLS) mechanism[31-34]. The SiNW bending sensor combines high piezoresistive sensitivity to small bending-induced strains with a sufficiently broad response range for wrist motion. When attached to the wrist, the sensor captures distinct tensile or compressive strain under different postures. Reversal of the bending direction changes the local sensor state from tension to compression, or vice versa, thereby producing distinguishable electrical responses for opposing wrist movements [Figure 1A]. When positioned on the dorsal side of the wrist, the sensor primarily captures flexion and extension, whereas placement on either the radial or ulnar side enables radial and ulnar deviation to be distinguished. Each mounting configuration therefore converts the corresponding pair of wrist movements into a single-channel time series. A compact wireless unit acquires this signal and transmits it to a computer via Bluetooth Low Energy (BLE) [Figure 1B]. The resulting time series is processed by a one-dimensional convolutional neural network (1D-CNN) to identify the wrist states associated with each mounting configuration. This study provides a simple wearable approach for monitoring wrist motion during resistance training.

EXPERIMENTAL

IPSLS growth of silicon nanowires and sensor fabrication

SiNW bending sensors were fabricated by directly growing morphology-programmed SiNWs on flexible polyimide (PI) substrates through the IPSLS mechanism. After ultrasonic cleaning, guiding edges with a depth of approximately 180 nm were defined by photolithography and oxygen-plasma ICP etching, followed by deposition of a 30-nm In catalyst layer. The samples were treated with H_2 plasma at 180 °C for 5 min, followed by deposition of a 15-nm a-Si:H precursor layer at 150 °C for 4 min. IPSLS growth was then activated by annealing at 200 °C for 1.5 h, allowing the In droplets to migrate along the guiding edges and form wavy SiNWs. Residual a-Si:H was removed by CF_4 reactive-ion etching. Finally, the SiNW surface oxide was removed using 4.0% HF solution, and Pt/Au (5/55 nm) electrodes were deposited to complete the devices.

Characterization and simulation

The morphology of the SiNW bending sensors was characterized by scanning electron microscopy (SEM). Electrical measurements were performed on a probe station using a high-precision source meter (Keithley 2635B, Tektronix, USA). The devices were mounted on a mechanical bending stage and subjected to controlled tensile and compressive bending under ambient conditions. The nominal surface strain was calculated as $\varepsilon = t/(2r)$, where t is the thickness of the PI substrate and r is the bending radius. The relative resistance change was calculated as $\Delta R/R0$. For quantitative sensitivity analysis, the effective gauge factor (GF) was determined from the slope of a linear fit to the initial approximately linear region of the $\Delta R/R0$–strain curve. Finite element analysis (FEA) was performed using the Solid Mechanics module in COMSOL Multiphysics (COMSOL AB, Sweden). The wavy SiNW geometry was constructed using composite curves and sweep operations, and the material properties of crystalline silicon were taken from the COMSOL material library, with a Young's modulus of 170 GPa and a Poisson's ratio of 0.28. Bending deformation was applied using a rigid connector with a prescribed displacement, and the resulting von Mises stress distribution was extracted to evaluate stress evolution within the SiNW during bending.

Signal acquisition and 1D-CNN classifier

Sensor signals were acquired using a custom-designed wireless circuit. A regulated bias voltage was applied to the SiNW sensor, and the resulting current was converted into a voltage signal by a transimpedance amplifier (TIA) with a 2 MΩ feedback resistor. The amplified signal was digitized using a 16-bit analog-to-digital converter (ADC) and transferred via an I^2C interface to an STM32WB5MMG microcontroller (STMicroelectronics, Switzerland), which transmitted the data to a host computer through Bluetooth Low Energy (BLE). The signals were segmented into 1s windows for classification. Only non-overlapping windows were used for model development to avoid data leakage, and the dataset was divided into training, validation, and test sets. The signals were z-standardized using parameters calculated exclusively from the training set, without introducing hand-engineered features. Classification was performed using a lightweight one-dimensional convolutional neural network (1D-CNN) comprising two convolutional layers, global average pooling, and a fully connected classification layer. Weighted cross-entropy loss was used to account for class imbalance, and the network was optimized using AdamW. Early stopping based on validation loss was applied during training, and the model with the lowest validation loss was retained for final evaluation.

RESULTS AND DISCUSSION

The structure and sensing mechanism of the SiNW bending sensor are illustrated in Figure 1C-E. The bending sensor consists of wavy SiNWs spanning two metal electrodes on a PI substrate [Figure 1C]. This morphology allows the conduction path to accommodate substrate curvature while preserving the large piezoresistive response associated with silicon[35,36]. FEA simulation was used to examine the spatial distribution of stress in the wavy SiNW channel [Figure 1D]. Bending the substrate inward produced a compressive strain across the SiNW channels, whereas bending it outward generated tensile strain. The stress distribution remained concentrated within the nanowire channels, converting the substrate curvature to the local deformation of the SiNWs. These opposite mechanical states are subsequently converted into electrical outputs through piezoresistive transduction [Figure 1E]. As illustrated schematically in Figure 1E, tensile strain increases the resistance, whereas compressive strain reduces the resistance. The polarity of the relative resistance change $\Delta R/R_0$ therefore provides direct information on bending direction, while its magnitude reflects the degree of local deformation. The combination of programmable geometry, mechanical compliance, and polarity-dependent piezoresistive response thus establishes the fundamental sensing principle.

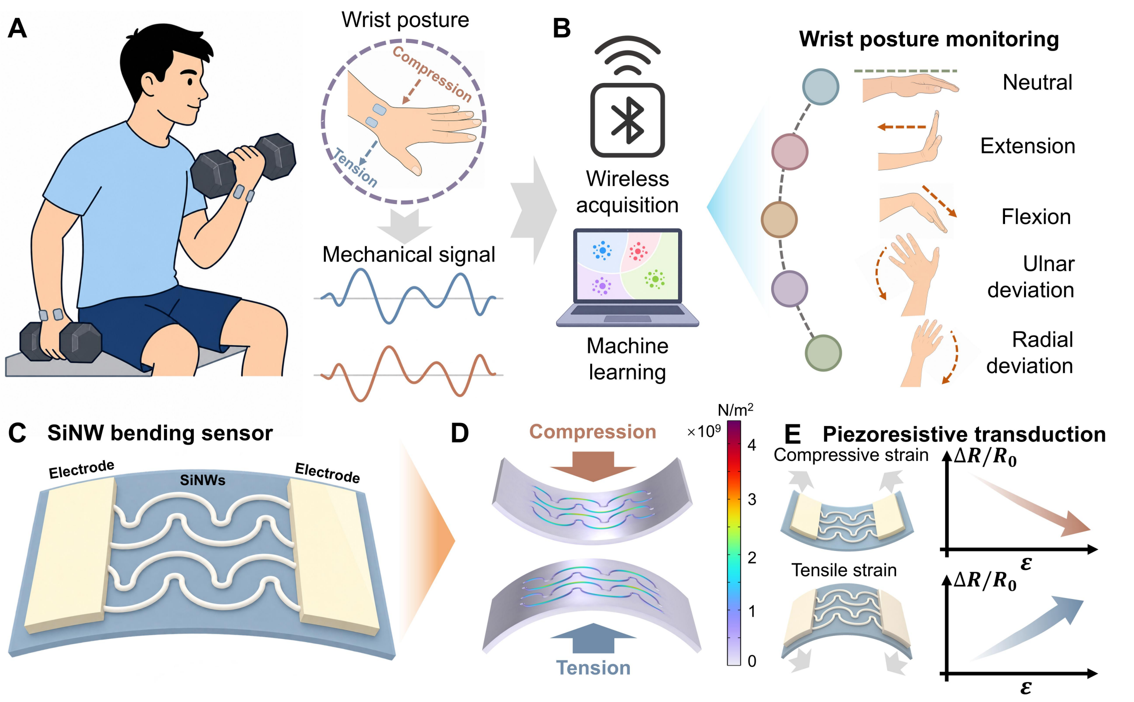

Figure 1. Concept and working principle of the SiNW bending sensor for wrist-posture monitoring. (A) Schematic illustration of the SiNW bending sensor attached to representative wrist locations for monitoring postures; (B) Wireless signal acquisition and

classification workflow for wrist-posture recognition; (C) Schematic structure of the SiNW bending sensor; (D) Stress distributions in the SiNW bending sensor obtained from finite-element analysis simulation; (E) Schematic illustration of the piezoresistive response under tensile and compressive bending.

To fabricate the morphology-programmable SiNW bending sensor, we adopted a direct, in situ route to grow SiNWs on a flexible PI substrate under low-temperature conditions through the IPSLS mechanism. Figure 2 summarizes the fabrication process, structural morphology, dimensional consistency, and representative on-wrist placement of the sensor. As shown in Figure 2A, in-plane guiding edges and the In catalyst region are first defined on the PI substrate. Hydrogen-plasma treatment converts the In film into droplets, after which an a-Si:H precursor layer is deposited. During subsequent thermal activation at approximately 200 °C, the In droplets absorb silicon species from the surrounding precursor and migrate laterally along the predefined guiding edges, continuously extruding SiNWs along their trajectories. After removal of the residual materials, Pt/Au electrodes are deposited to establish electrical contact with the SiNW channels. SEM characterization confirms the formation of continuous wavy SiNW structures [Figure 2B]. The enlarged image in Figure 2C further resolves the wavy nanowire path without obvious discontinuities. Additional optical and SEM images are provided in Supplementary Figure 1, further showing multiple fabricated sensor units and the large-area distribution of wavy SiNW arrays across the patterned regions. The diameter distribution in Figure 2D is concentrated mainly between approximately 120 and 150 nm, with Gaussian fitting giving a characteristic diameter of 136 ± 5 nm. Figure 2E shows representative placements of the fabricated sensor to the dorsal, ulnar, and radial sides of the wrist, illustrating the conformal integration of the flexible device with the curved wrist surface.

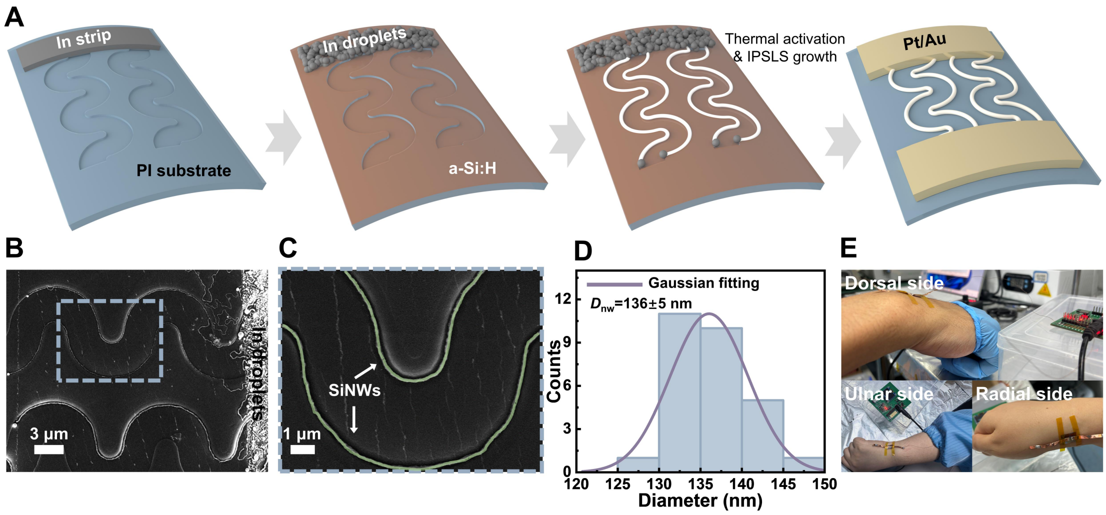

Figure 2. Fabrication, morphology, and representative on-wrist placement of the SiNW bending sensor. (A) Fabrication process of the morphology-programmable SiNW bending sensor through the IPSLS mechanism; (B) Representative SEM image of the wavy SiNW channels on the PI substrate; (C) Enlarged SEM image of the boxed region in (B), highlighting the continuous wavy SiNW morphology; (D) SiNW diameter distribution with Gaussian fitting; (E) Photographs of the sensor attached to the dorsal, ulnar, and radial sides of the wrist.

The response of the SiNW bending sensor under compression was first characterized, as shown in Figure 3A-D. When the PI substrate was bent toward the SiNW side, the sensing channel was subjected to compressive deformation [Figure 3A]. The *I-V* curves remained approximately linear from -0.10 to 0.10 V at all applied strains, while their slopes gradually increased with increasing compression [Figure 3B]. This indicates a progressive decrease in the resistance of the SiNW channel without an obvious change in the overall conduction behavior. The same trend is observed in the dynamic measurements. At a fixed bias of 0.1 V, the current increased stepwise as the compressive strain was increased, and each strain level produced a clearly distinguishable current state [Figure 3C]. Figure 3D summarizes the corresponding relative resistance change $\Delta R/R_0$ in the initial approximately linear portion. This low-strain regime is relevant to the wrist-posture application considered in this work. Within this region, $\Delta R/R_0$ decreases nearly

DOI: 10.20517/scierxiv202609.0756.v1

linearly with increasing compression, giving an effective GF magnitude of approximately 32.

An opposite electrical response was observed when the bending direction was reversed and the SiNW channel was subjected to tensile deformation [Figure 3E-H]. The *I-V* characteristics remained approximately linear throughout the tested strain range, but the slopes decreased progressively with increasing tensile strain [Figure 3F], corresponding to an increase in channel resistance. This trend is also evident in the time-dependent current measurements at a bias of 0.1 V. As the tensile strain increased, the current decreased stepwise and formed distinct plateaus for different deformation levels [Figure 3G]. Figure 3H presents the initial approximately linear region of the $\Delta R/R_0$-strain curve for sensitivity evaluation. In this low-strain range, $\Delta R/R_0$ increases nearly linearly with tensile strain, giving an effective GF of approximately 170. Comparison of Figure 3D and H therefore shows that compression and tension generate resistance changes of opposite polarity, while the tensile state exhibits a larger effective sensitivity within the low-strain regime. This polarity-dependent response enables the two bending directions to be distinguished using a single electrical channel.

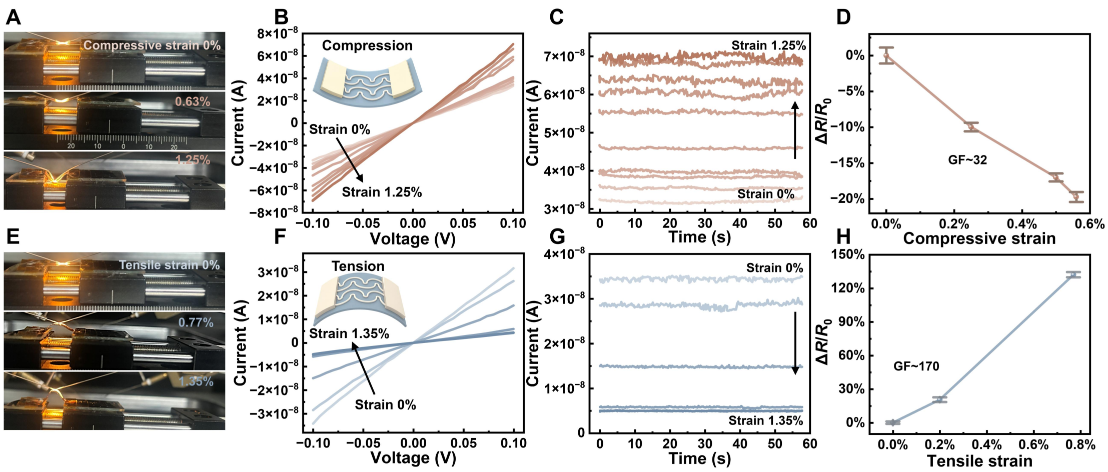

Figure 3. Electrical characterization of the SiNW bending sensor under compression and tension. (A) Photographs of the SiNW bending sensor subjected to compressive strain; (B) *I-V* characteristics of the SiNW bending sensor measured under compressive strain;

DOI: 10.20517/scierxiv202609.0756.v1

(C) Time-dependent current responses recorded at an input bias of V_{in} = 0.1 V; (D) Relative resistance change $\Delta R/R_0$ versus compressive strain in the initial approximately linear region, with error bars and the corresponding effective GF; (E) Photographs of the SiNW bending sensor subjected to tensile strain; (F) *I-V* characteristics of the SiNW bending sensor measured under tensile strain; (G) Time-dependent current responses recorded at an input bias of V_{in} = 0.1 V; (H) Relative resistance change $\Delta R/R_0$ versus tensile strain in the initial approximately linear region, with error bars and the corresponding effective GF.

The difference in effective sensitivity between tension and compression likely arises from the combined effects of strain transfer through the wavy SiNW geometry and the piezoresistive response of c-Si. Mechanical stress alters the band structure and carrier transport in c-Si, thereby changing its resistivity[37-39]. In this work, the GF is evaluated using the nominal bending strain of the PI substrate and therefore represents the effective sensitivity of the complete device rather than the intrinsic piezoresistive coefficient of the SiNWs. Because the SiNWs follow a wavy path, the applied substrate strain is not transferred directly into uniform axial strain along the nanowire. Instead, part of the deformation can be accommodated through changes in local curvature[40,41]. Under tension, the curved segments tend to straighten, allowing a larger fraction of the substrate deformation to be transferred into axial stretching of the nanowire. Under compression, deformation can be accommodated to a greater extent by increased curvature. The asymmetry between tension and compression may arise from the distinct geometric responses of wavy silicon structures under compression and tension[42]. This geometry-dependent deformation may also contribute to the higher effective sensitivity observed under tension in the initial linear regime[16,43]. At larger deformation, continued geometric reconfiguration can introduce a nonlinear relationship between substrate strain and nanowire strain. Because such larger bending is not the operating condition for the wrist-posture measurements, these nonlinear regions are not used for additional GF quantification. The opposite low-strain resistance responses under tension and compression therefore provide the sensing basis for distinguishing wrist movements.

Before wrist-posture monitoring, the stability of the SiNW bending sensor was evaluated under cyclic deformation. Figure 4A shows the current response under repeated 0.8% compressive strain. The current increases during compression and returns toward its initial level after release, while the response amplitude remains similar over cycles. The tensile response was further examined under 0.8% strain for 50 loading cycles [Figure 4B] without obvious progressive degradation or baseline drift. During each cycle, the relative resistance change reaches a comparable peak and then recovers after unloading. The enlarged traces in the inset show similar waveform shapes and peak values throughout the test. These results indicate that the SiNW channel maintains stable electrical transduction during repeated compression and tension. Such repeatability is important for wrist monitoring because the sensor experiences continuous bending and recovery during natural motion rather than isolated static deformation. The cyclic measurements therefore confirm that the programmed SiNW channel can preserve both its response direction and signal amplitude under repetitive loading, providing a reliable basis for subsequent acquisition of posture-dependent wrist signals.

We then evaluated the capability of the SiNW bending sensor to monitor wrist motion. When the sensor was attached to the dorsal side of the wrist, repeated wrist extension produced reproducible current changes from the neutral position [Figure 4C], whereas wrist flexion generated a response in the opposite direction [Figure 4D]. This behavior agrees with the controlled bending measurements in Figure 3, where tensile and compressive deformation produce resistance changes with opposite polarities. During wrist motion, extension and flexion create different local curvature states at the dorsal attachment site and therefore drive the SiNW channel toward opposite deformation conditions[25,44]. The two movements can consequently be distinguished from both the

DOI: 10.20517/scierxiv202609.0756.v1

direction and magnitude of the electrical response. Differences in peak amplitude and waveform shape are observed among individual cycles, mainly because the bending angle and movement speed vary between natural motions. Nevertheless, the response direction remains clear throughout the repeated measurements. The same placement-dependent principle applies to the ulnar side of the wrist, where radial and ulnar deviation produce opposite local bending states.

For wrist posture recognition, the continuously recorded signals were processed using the workflow shown in Figure 4E. The ADC signal was divided into fixed 1s windows, and the resulting time-series segments were fed into a 1D-CNN. For the sensor placed on the dorsal side of the wrist, the model classified wrist flexion, neutral position, and wrist extension with an overall accuracy of approximately 98.0%, as shown by the confusion matrix in Figure 4F. For the sensor placed on the radial or ulnar side of the wrist, a separate model was used to distinguish radial deviation, neutral position, and ulnar deviation, achieving an accuracy of approximately 97.8% [Figure 4G]. Only a small number of samples were assigned to incorrect classes in either task. The corresponding training and validation loss curves are provided in Figure S2. The two losses decrease during training and remain close as the models converge, without a clear divergence between the training and validation sets, indicating no evident overfitting. These results show that the posture-dependent signals obtained from both wrist locations contain sufficient temporal information for reliable recognition.

The classification performance of the 1D-CNN was further compared with four conventional models: random forest (RF), logistic regression (LR), support vector machine with a radial basis function kernel (RBF-SVM), and polynomial regression (PR) [Figure 4H]. The comparison was performed for the posture-recognition tasks based on signals collected from the dorsal and radial/ulnar sides of the wrist. The 1D-CNN achieved the highest overall classification accuracy of approximately 97.5%, followed closely by RF at 96.5%. LR and RBF-SVM both reached approximately 95.8%, while PR showed a lower classification accuracy. The relatively small performance gap among the better-performing models also suggests that the electrical signals associated with different wrist postures are intrinsically well separated, rather than becoming distinguishable only after complex model processing. Nevertheless, the 1D-CNN provided the best overall result while operating directly on the segmented time-series signals. Its convolutional layers capture short-term variations in signal magnitude and waveform evolution within each window, which are useful for distinguishing dynamic wrist movements[18,45].

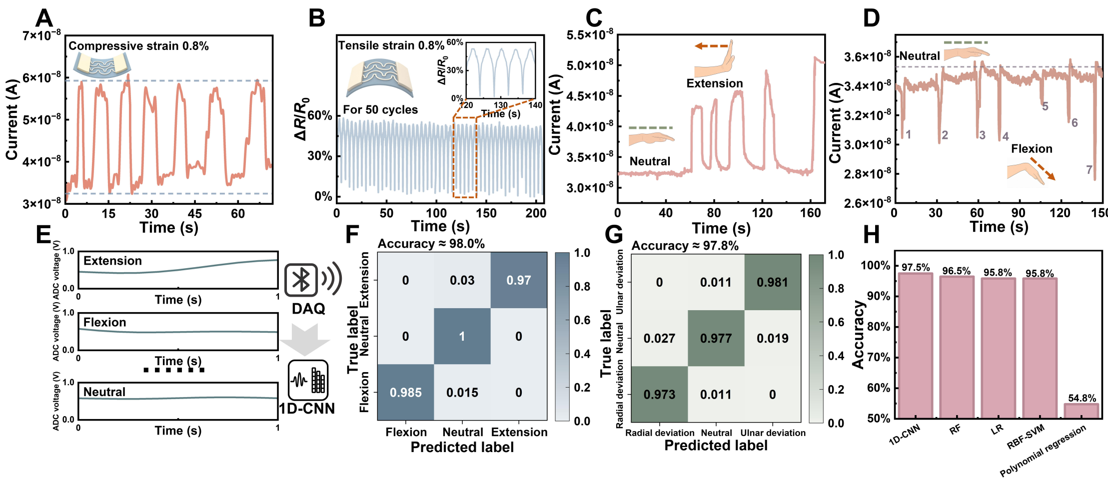

Figure 4. Comprehensive characterization of the bending sensor toward wrist posture monitoring. (A) Time-dependent current response under repeated 0.8% compressive strain; (B) Relative resistance change $\Delta R/R_0$ during 50 tensile loading cycles at 0.8% strain, the inset shows an enlarged view of representative loading cycles; (C, D) Time-dependent current responses during repeated transitions between the neutral wrist position and (C) wrist extension and (D) wrist flexion; (E) Signal-processing workflow in which the continuous ADC voltage is segmented into fixed 1s windows and fed into a 1D-CNN; (F) Confusion matrix for classification of wrist flexion, neutral position, and wrist extension; (G) Confusion matrix for classification of radial deviation, neutral position, and ulnar deviation; (H) Comparison of classification accuracy among the 1D-CNN, random forest, logistic regression, RBF-SVM, and polynomial regression models.

DOI: 10.20517/scierxiv202609.0756.v1

CONCLUSION

In this work, we developed a morphology-programmable SiNW bending sensor for wearable wrist-posture monitoring. The SiNWs were grown directly on a flexible PI substrate through the IPSLS process, allowing wavy sensing channels to be defined without transfer printing. The resulting device showed clear and opposite resistance responses under tensile and compressive bending. For sensitivity evaluation, only the initial approximately linear strain regions were considered, giving effective GF magnitudes of approximately 32 under compression and 170 under tension. Repeated bending tests further showed stable and reversible electrical responses. The bidirectional response allowed wrist movements to be distinguished according to sensor attachment position. A sensor placed on the dorsal side of the wrist resolved flexion, neutral position, and extension, whereas placement on the radial or ulnar side resolved radial deviation, neutral position, and ulnar deviation. After wireless acquisition and 1s signal segmentation, a lightweight 1D-CNN achieved classification accuracies of approximately 98.0% and 97.8% for the two three-class tasks. The close training and validation loss curves further showed no evident overfitting during model training. The present system uses one sensing location to monitor one main wrist-motion plane, and further work is needed to combine multiple sensing locations and evaluate performance across different users and exercise conditions. Nevertheless, the combination of programmable SiNW growth, direction-dependent bending response, and simple single-channel signal processing provides a practical route toward compact wearable systems for wrist-posture monitoring.

DECLARATIONS

Authors' contributions

Conception of the idea, experimental design, and supervision of the research project: Wang S, Song X, Yu L;

Conduct of the experiments and device fabrication: Wang S, Song X, Qin Z, Gu Y;

Data analysis and manuscript writing: Wang S, Qin Z, Song X;

All authors discussed the results and commented on the paper.

Availability of data and materials

The data supporting the findings of this study are available in the Supplementary Materials. Additional data and materials are available from the corresponding author upon reasonable request.

AI and AI-assisted tools statement

Not applicable.

Financial support and sponsorship

This work was supported by the National Natural Science Foundation of China for Distinguished Young Scholars Grant No. 62325403, National Natural Science Foundation of China Grant 62504103, the Basic Research Program of Jiangsu BK20251214, Natural Science Foundation of Jiangsu Province Grant BK20230498.

Conflicts of interest

The authors declare that they have no conflicts of interest.

Ethical approval and consent to participate

This study involved only non-invasive data collection using a wearable sensor attached to the skin during normal wrist movements, without any invasive procedures or additional health risks to the participants. In accordance with Article 32 of China's *Measures for Ethical Review of Life Science and Medical Research Involving Human Beings*, the study met the conditions for exemption from ethical review. All participants were informed of the study procedures before participation, and written informed consent was obtained from each participant.

Consent for publication

Not applicable.

Copyright

REFERENCES

1. Keogh, J.W.; Winwood, P.W. The epidemiology of injuries across the weight-training sports. *Sports Medicine* **2017**, *47*, 479-501.[PMID: 27328853 DOI: 10.1007/s40279-016-0575-0]

2. Coffey, K.; Pezzullo, L.; Nixon, R.M.; Bolling, J.; Vincent, H.K. A 10-Year Analysis of Resistance Training-Related Injuries Treated in Emergency Departments: Are Patterns Shifting With More Participation of Women Over Time? *The Journal of Strength & Conditioning Research* **2026**, *40*, e1-e8.[PMID: 41118234 PMCID: PMC12688451 DOI: 10.1519/JSC.0000000000005268]

3. Aasa, U.; Svartholm, I.; Andersson, F.; Berglund, L. Injuries among weightlifters and powerlifters: a systematic review. *British Journal of Sports Medicine* **2017**, *51*, 211-9.[PMID: 27707741 DOI: 10.1136/bjsports-2016-096037]

4. Viegas, S.; Tencer, A.; Cantrell, J.; et al. Load transfer characteristics of the wrist. Part I. The normal joint. *The Journal of Hand Surgery* **1987**, *12*, 971-8.[PMID: 3693853 DOI: 10.1016/s0363-5023(87)80093-x]

5. McGorry, R.W.; Fallentin, N.; Andersen, J.H.; et al. Effect of grip type, wrist motion, and resistance level on pressures within the carpal tunnel of normal wrists. *Journal of Orthopaedic Research* **2014**, *32*, 524-30.[PMID: 24391059 PMCID: PMC4305197 DOI: 10.1002/jor.22571]

6. Adams, B.D.; Holley, K.A. Strains in the articular disk of the triangular fibrocartilage complex: a biomechanical study. *The Journal of Hand Surgery* **1993**, *18*, 919-25.[PMID: 8228070 DOI: 10.1016/0363-5023(93)90066-C]

7. Hart, R.; Smith, H.; Zhang, Y. Systematic review of automatic assessment systems for

resistance-training movement performance: A data science perspective. *Computers in Biology and Medicine* **2021**, *137*, 104779.[PMID: 34454166 DOI: 10.1016/j.compbiomed.2021.104779]

8. Mathis, A.; Schneider, S.; Lauer, J.; Mathis, M.W. A primer on motion capture with deep learning: principles, pitfalls, and perspectives. *Neuron* **2020**, *108*, 44-65.[PMID: 33058765 DOI: 10.1016/j.neuron.2020.09.017]

9. Shin, H.-S.; Kim, J.; Fadell, N.; et al. Soft, skin-interfaced wireless electrogoniometry systems for continuous monitoring of finger and wrist joints. *Nature Communications* **2025**, *16*, 4426.[PMID: 40360513 PMCID: PMC12075735 DOI: 10.1038/s41467-025-59619-z]

10. Lu, G.; Kim, S.; Chen, X.; et al. Hand tracking using wearable wrist imaging. *Nature Electronics* **2026**, 1-15.[DOI: 10.1038/s41928-026-01594-4]

11. Kim, D.; Jin, Y.; Cho, H.; et al. Learning-based 3D human kinematics estimation using behavioral constraints from activity classification. *Nature Communications* **2025**, *16*, 3454.[PMID: 40216761 PMCID: PMC11992036 DOI: 10.1038/s41467-025-58624-6]

12. Laidig, D.; Seel, T. VQF: Highly accurate IMU orientation estimation with bias estimation and magnetic disturbance rejection. *Information Fusion* **2023**, *91*, 187-204.[DOI: 10.1016/j.inffus.2022.10.014]

13. Moin, A.; Zhou, A.; Rahimi, A.; et al. A wearable biosensing system with in-sensor adaptive machine learning for hand gesture recognition. *Nature Electronics* **2021**, *4*, 54-63.[DOI: 10.1038/s41928-020-00510-8]

14. Xia, H.; Zhang, Y.; Rajabi, N.; et al. Shaping high-performance wearable robots for human motor and sensory reconstruction and enhancement. *Nature Communications* **2024**, *15*, 1760.[PMID: 38409128 PMCID: PMC10897332 DOI: 10.1038/s41467-024-46249-0]

15. Guo, J.; Tong, Y.; Guo, C.; et al. In-situ real-time monitoring of muscle energetics with soft neural-mechanical wearable sensing. *Soft Science* **2025**, *5*, 20.[DOI: 10.20517/ss.2024.75]

16. Kim, J.; Lee, M.; Shim, H.J.; et al. Stretchable silicon nanoribbon electronics for skin prosthesis. *Nature Communications* **2014**, *5*, 5747.[PMID: 25490072 DOI: 10.1038/ncomms6747]

17. Zhang, H.; Liu, D.; Lee, J.-H.; et al. Anisotropic, wrinkled, and crack-bridging structure for ultrasensitive, highly selective multidirectional strain sensors. *Nano-Micro Letters* **2021**, *13*, 122.[PMID: 34138324 PMCID: PMC8096879 DOI: 10.1007/s40820-021-00615-5]

18. Cheng, A.; Li, X.; Li, D.; et al. An intelligent hybrid-fabric wristband system enabled by thermal encapsulation for ergonomic human-machine interaction. *Nature Communications* **2025**, *16*, 591.[PMID: 39799116 PMCID: PMC11724971 DOI: 10.1038/s41467-024-55649-1]

19. Yan, C.; Li, X.; Wang, X.; et al. Extremely Stable, Multidirectional, All-in-One Piezoelectric Bending Sensor with Cycle up to Million Level. *Advanced Functional Materials* **2024**, *34*, 2409093.[DOI: 10.1002/adfm.202409093]

20. Zhong, L.; Tian, X.; Wang, J.-Y.; et al. Calibration-free optical waveguide bending sensor for soft robots. *Soft Science* **2025**, *5*, 8.[DOI: 10.20517/ss.2024.52]

21. Liu, Y.; Yiu, C.; Song, Z.; et al. Electronic skin as wireless human-machine interfaces for robotic VR. *Science Advances* **2022**, *8*, eabl6700.[DOI: 10.1126/sciadv.abl6700]

22. Kaidarova, A.; Khan, M.A.; Marengo, M.; et al. Wearable multifunctional printed graphene sensors. *npj Flexible Electronics* **2019**, *3*, 15.[DOI: 10.1038/s41528-019-0061-5]

23. Li, Z.; Hu, F.; Chen, Z.; et al. Fiber-junction design for directional bending sensors. *npj Flexible Electronics* **2021**, *5*, 4.[DOI: 10.1038/s41528-021-00102-2]

24. Wang, W.; Bo, X.; Li, W.; et al. Triboelectric Bending Sensors for AI-Enabled Sign Language Recognition. *Advanced Science* **2025**, *12*, 2408384.[DOI: 10.1002/advs.202408384]

25. Jeong, S.-M.; Son, M.; Kang, Y.; Yang, J.; Lim, T.; Ju, S. Development of multi-angle fiber array for accurate measurement of flexion and rotation in human joints. *npj Flexible*

Electronics **2021**, *5*, 35.[DOI: 10.1038/s41528-021-00131-x]

26. Liu, H.; Takakuwa, M.; Yamamoto, M.; et al. Ultrathin bending sensor with ultrahigh robustness and reliability for robotic applications. *npj Flexible Electronics* **2025**, *9*, 123.[DOI: 10.1038/s41528-025-00498-1]

27. Takamatsu, S.; Takakuwa, M.; Fukuda, K.; et al. Flexible no-drift data glove using ultrathin silicon for the metaverse. *Device* **2025**, *3*, 100686.[DOI: 10.1016/j.device.2024.100686]

28. Rogers, J.A.; Someya, T.; Huang, Y. Materials and mechanics for stretchable electronics. *Science* **2010**, *327*, 1603-7.[PMID: 20339064 DOI: 10.1126/science.1182383]

29. Hu, B.; Xu, D.; Shao, Y.; et al. Ultrathin crystalline silicon-based omnidirectional strain gauges for implantable/wearable characterization of soft tissue biomechanics. *Science Advances* **2024**, *10*, eadp8804.[PMID: 39383239 PMCID: PMC11463283 DOI: 10.1126/sciadv.adp8804]

30. Yan, L.; Liu, Z.; Wang, J.; Yu, L. Integrating hard silicon for high-performance soft electronics via geometry engineering. *Nano-Micro Letters* **2025**, *17*, 218.[PMID: 40227525 PMCID: PMC11996752 DOI: 10.1007/s40820-025-01724-1]

31. Song, X.; Qin, Z.; Wang, S.; et al. Morphology-Programmable Orthogonally Aligned Silicon Nanowire Arrays for Integrated Strain-Temperature Bimodal Sensing. *Nano Letters* **2026**, *26*, 6955-64.[PMID: 42170943 DOI: 10.1021/acs.nanolett.6c00850]

32. Song, X.; Gu, Y.; Wang, S.; et al. Scalable integration of high sensitivity strain sensors based on silicon nanowire spring array directly grown on flexible polyimide films. *Nano Letters* **2025**, *25*, 2290-7.[PMID: 39881565 DOI: 10.1021/acs.nanolett.4c05553]

33. Yu, L.; Alet, P.-J.; Picardi, G.; Roca i Cabarrocas, P. An in-plane solid-liquid-solid growth mode for self-avoiding lateral silicon nanowires. *Physical Review Letters* **2009**, *102*, 125501.[PMID: 19392293 DOI: 10.1103/PhysRevLett.102.125501]

34. Yu, L.; Oudwan, M.; Moustapha, O.; Fortuna, F.; Roca i Cabarrocas, P. Guided growth of in-plane silicon nanowires. *Applied Physics Letters* **2009**, *95*, 113106.[DOI: 10.1063/1.3227667]

35. Dong, T.; Sun, Y.; Zhu, Z.; et al. Monolithic integration of silicon nanowire networks as a soft wafer for highly stretchable and transparent electronics. *Nano letters* **2019**, *19*, 6235-43.[DOI: 10.1021/acs.nanolett.9b02291]

36. Huang, S.; Zhang, B.; Shao, Z.; et al. Ultraminiaturized stretchable strain sensors based on single silicon nanowires for imperceptible electronic skins. *Nano Letters* **2020**, *20*, 2478-85.[PMID: 32142295 DOI: 10.1021/acs.nanolett.9b05217]

37. He, R.; Yang, P. Giant piezoresistance effect in silicon nanowires. *Nature Nanotechnology* **2006**, *1*, 42-6.[PMID: 18654140 DOI: 10.1038/nnano.2006.53]

38. Smith, C.S. Piezoresistance effect in germanium and silicon. *Physical Review* **1954**, *94*, 42.[DOI: 10.1103/PhysRev.94.42]

39. Nakamura, K.; Isono, Y.; Toriyama, T.; Sugiyama, S. Simulation of piezoresistivity in n-type single-crystal silicon on the basis of the first-principles band structure. *Physical Review B—Condensed Matter and Materials Physics* **2009**, *80*, 045205.[DOI: 10.1103/PhysRevB.80.045205]

40. Ryu, S.Y.; Xiao, J.; Park, W.I.; et al. Lateral buckling mechanics in silicon nanowires on elastomeric substrates. *Nano Letters* **2009**, *9*, 3214-9.[PMID: 19670847 DOI: 10.1021/nl901450q]

41. Xu, F.; Lu, W.; Zhu, Y. Controlled 3D buckling of silicon nanowires for stretchable electronics. *ACS Nano* **2011**, *5*, 672-8.[PMID: 21189041 DOI: 10.1021/nn103189z]

42. Khang, D.-Y.; Jiang, H.; Huang, Y.; Rogers, J.A. A stretchable form of single-crystal silicon for high-performance electronics on rubber substrates. *Science* **2006**, *311*, 208-12.[PMID: 16357225 DOI: 10.1126/science.1121401]

43. Wu, H.; Liu, B.; Wang, S.; et al. Geometry-Tunable Stretchability and Piezoresistive Response in Growth-Programmable In-Plane Silicon Nanowire Springs. *The Journal of Physical Chemistry Letters* **2026**.[PMID: 42478788 DOI: 10.1021/acs.jpclett.6c01857]

44. Liu, H. The Touch-Code Glove: a multimodal mapping interface with triboelectric-digital encoding for intuitive robot training. *Soft Science* **2025**, *5*, 60.[DOI: 10.20517/ss.2025.68]

45. Wen, F.; Zhang, Z.; He, T.; Lee, C. AI enabled sign language recognition and VR space bidirectional communication using triboelectric smart glove. *Nature Communications* **2021**, *12*, 5378.[PMID: 34508076 PMCID: PMC8433305 DOI: 10.1038/s41467-021-25637-w]